Article

TRANSPARENT PROCESS

THE EMBO JOURNAL

Identification and function of conformational dynamics in the multidomain GTPase dynamin

Saipraveen Srinivasan[1], Venkatasubramanian Dharmarajan[2], Dana Kim Reed[1], Patrick R Griffin[2] & Sandra L Schmid[1,*]

Abstract

Vesicle release upon endocytosis requires membrane fission, catalyzed by the large GTPase dynamin. Dynamin contains five domains that together orchestrate its mechanochemical activity. Hydrogen–deuterium exchange coupled with mass spectrometry revealed global nucleotide- and membrane-binding-dependent conformational changes, as well as the existence of an allosteric relay element in the $\alpha 2^S$ helix of the dynamin stalk domain. As predicted from structural studies, FRET analyses detect large movements of the pleckstrin homology domain (PHD) from a 'closed' conformation docked near the stalk to an 'open' conformation able to interact with membranes. We engineered dynamin constructs locked in either the closed or open state by chemical cross-linking or deletion mutagenesis and showed that PHD movements function as a conformational switch to regulate dynamin self-assembly, membrane binding, and fission. This PHD conformational switch is impaired by a centronuclear myopathy-causing disease mutation, S619L, highlighting the physiological significance of its role in regulating dynamin function. Together, these data provide new insight into coordinated conformational changes that regulate dynamin function and couple membrane binding, oligomerization, and GTPase activity during dynamin-catalyzed membrane fission.

Keywords centronuclear myopathy; clathrin-mediated endocytosis; hydrogen–deuterium exchange; membrane fission; pleckstrin homology domain

Subject Categories Membrane & Intracellular Transport; Structural Biology

DOI 10.15252/embj.201593477 | Received 11 November 2015 | Revised 9 December 2015 | Accepted 11 December 2015 | Published online 18 January 2016

The EMBO Journal (2016) 35: 443–457

Introduction

Dynamic membrane remodeling events in biological systems are the result of highly orchestrated interactions between proteins and the underlying lipid membrane (Chernomordik & Kozlov, 2003). The dynamin superfamily of mechanochemical GTPases catalyze such membrane remodeling events, for example, fission, tubulation, and fusion (Praefcke & McMahon, 2004). Dynamin, its prototypical member, catalyzes membrane fission in clathrin-mediated endocytosis (CME) (Schmid & Frolov, 2011; Ferguson & De Camilli, 2012; Morlot & Roux, 2013). Dynamin consists of an N-terminal GTPase domain, the middle and GTPase effector (GED) domains that together form a four-helical bundled 'stalk' required for higher-order assembly, a PtdIns(4,5)P_2-targeting pleckstrin homology domain (PHD), and a C-terminal proline and arginine-rich domain (PRD) that interacts with Src-homology 3 (SH3) domain-containing proteins (Fig 1A). The N- and C-terminal helices of the G domain and the C-terminal helix of the GED together form the three-helix bundle signaling element (BSE) (Chappie *et al*, 2009), which akin to the lever arm of motor proteins, transmits nucleotide-driven conformational changes from the G domain to the stalk (Mattila *et al*, 2015).

The BSE and PHD are mobile elements necessary for dynamin function. The BSE undergoes a ~70° rigid body motion relative to the G domain during cycles of GTP binding and hydrolysis (Chappie *et al*, 2011; Mattila *et al*, 2015). Cross-linking the BSE against the G domain locks dynamin in its GDP•AlF_4^--bound transition-state conformation. Under these conditions, dynamin can assemble onto lipid templates and drive the formation of hemi-fission intermediates, even in the absence of GTP hydrolysis, but cannot catalyze fission (Mattila *et al*, 2015). Upon recruitment of dynamin to membranes, the PHD stably inserts its hydrophobic variable loops, VL1 and VL3, into the outer leaflet of the lipid bilayer. In combination with dynamin's assembly into a helical scaffold, wedging and tilting of the PHD drive curvature generation (Ramachandran & Schmid, 2008; Ramachandran *et al*, 2009) and have been proposed to be necessary for hemi-fission and subsequent fission (Shnyrova *et al*, 2013; Sundborger *et al*, 2014; Mattila *et al*, 2015). Recent evidence suggests that the PHD wedging activity may be coupled to GTP hydrolysis (Mehrotra *et al*, 2014) and increases when the BSE is locked in the transition state (Mattila *et al*, 2015). How information regarding the nucleotide-bound state of the G domain is transmitted to the PHD is not known.

In crystal structures of dynamin lacking only its PRD, the PHD is connected to the base of the stalk via unresolved loops extending from its N- and C-termini (Faelber *et al*, 2011; Ford *et al*, 2011).

1 Department of Cell Biology, UT Southwestern Medical Center, Dallas, TX, USA
2 Department of Molecular Therapeutics, The Scripps Research Institute, Jupiter, FL, USA
*Corresponding author. Tel: +1 214 648 3948; E-mail: sandra.schmid@utsouthwestern.edu

© 2016 The Authors

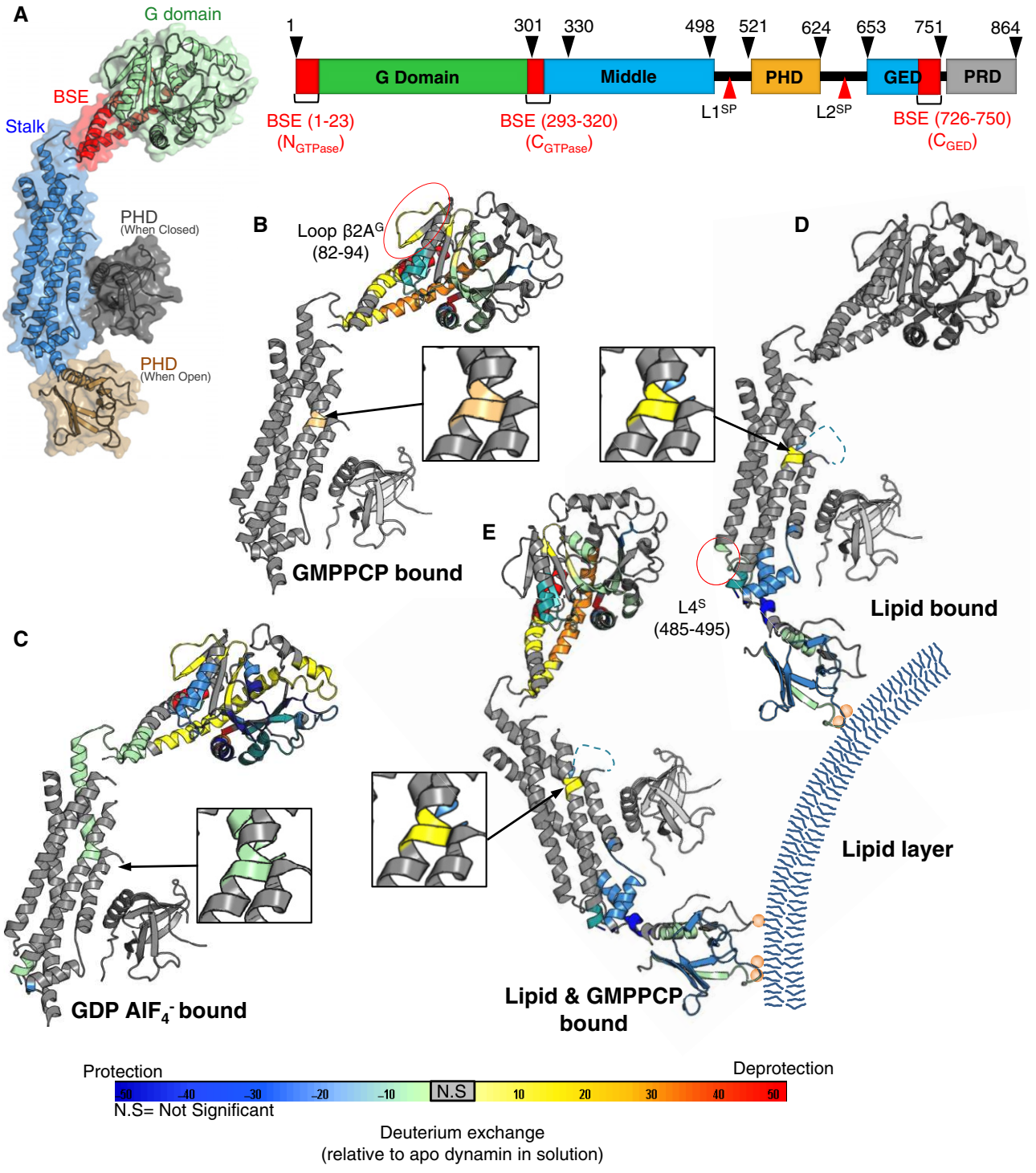

Figure 1. Hydrogen–deuterium exchange kinetics reveal long-range nucleotide- and/or membrane-binding-driven conformational changes in dynamin.

A Crystal structure of a dynamin monomer (PDB ID: 3SNH) and corresponding color-coded linear domain architecture of dynamin. The PHD is shown in both the closed (3SNH, solution structure) and open (3ZYS, cryo-EM reconstruction of membrane-bound dynamin) states. The approximate locations of terminal residues flanking different functional domains are identified with black arrowheads. The positions of the $L1^{SP}$ and $L2^{SP}$ loops are identified by red arrowheads.

B–E Changes in HDX behavior for dynamin analyzed (B) in solution in the presence of GMPPCP, (C) in solution in the presence of GDP•AlF_4^-, (D) membrane bound, or (E) membrane bound in the presence of GMPPCP and mapped onto the structures of dynamin monomers. Color coding (see scale below) shows the extent of solvent exchange relative to apo dynamin in solution. All HDX-MS data shown represent an average of three replicates and are color-coded from red to blue with warm colors representing increased conformational dynamics (red being the highest D_2O uptake) and cool colors representing decreased conformational dynamics (blue being the lowest D_2O uptake). Gray indicates no statistically significant change between the two states. Quantitative data on the individual peptides used to generate this map are provided in Appendix Figs S1–S4.

 © 2016 The Authors

Thus, there remained some ambiguity as to the connectivity between these domains (Faelber *et al*, 2011; Ford *et al*, 2011) and the positioning of the PHD. The recently solved crystal structure of dynamin-3 (Dyn3) tetramers revealed a pair of dimers, each containing an outer and an inner molecule (Reubold *et al*, 2015). The two PHDs originating from the outer molecules were docked against the stalk. In this position, referred to as the 'closed' state, the PHDs would be unable to bind liposomes; moreover, they obstruct the protein interface ('interface 3') that is required for further higher-order dynamin assembly. In contrast, the PHDs from the inner molecules were unresolved, suggesting a high degree of conformational flexibility. From these data, the authors suggest that the PHD plays an auto-inhibitory role in regulating dynamin assembly at the membrane (Reubold *et al*, 2015). Whether these conformational changes occur in solution, and if so their functional consequence, remains to be demonstrated.

Cryo-EM densities of the dynamin scaffold on lipid templates assign PHDs to the base of the stalk, where they insert into the outer leaflet of the lipid bilayer (Chappie *et al*, 2011), herein referred to as the 'open' state. If both these arrangements are correct, then the PHD must undergo a significant conformational rearrangement from the closed to the open state upon lipid binding to facilitating higher-order assembly and scaffolding. Interestingly, in the super-constricted state, alternating PHDs are tilted ~45° out of the membrane, again suggesting conformational flexibility even within the membrane-bound dynamin scaffolds (Sundborger *et al*, 2014).

Here, we surveyed site-specific fluctuations of the dynamin's conformational dynamics induced by nucleotide and membrane interactions using hydrogen/deuterium exchange (HDX). Site-specific FRET labeling, chemical cross-linking, and mutagenesis approaches provided evidence for a regulatory conformational switch resulting from a large change in the PHD orientation that affects GTP hydrolysis, oligomerization, membrane binding, and fission. Further, we show that the PHD conformational switch is altered by a common centronuclear myopathy (CNM) disease-causing mutation, S619L, residing at the PHD–stalk interface (Durieux *et al*, 2010; Kenniston & Lemmon, 2010), providing direct evidence for its physiological importance in regulating dynamin function.

Results and Discussion

HDX reveals site-specific conformational changes driven by nucleotide binding

Consensus is building that dynamin-catalyzed membrane fission requires its self-assembly to constrict membrane necks and assembly-stimulated GTP hydrolysis to drive global conformational changes (Chappie & Dyda, 2013). Thus far, the only GTPase-driven conformational change observed is the large-scale movement of the BSE, first predicted by structural studies of a truncated G domain-BSE construct (Chappie *et al*, 2011), and later confirmed by FRET measurements in intact dynamin (Mattila *et al*, 2015). How and whether GTP-dependent conformational changes of the BSE are transmitted to distal regions of the protein remains unknown. We sought evidence for long-range conformation changes in purified $Dyn1^{WT}$ by applying HDX coupled with mass spectrometry (HDX-MS) (Fig EV1). Perturbation in time-dependent differential deuterium uptake profiles (measured as changes in the number of amide hydrogens exchanged with solvent deuterium between two states; for example, apo versus ligand bound) can both identify ligand-binding sites as well as indicate long-range allosteric conformational alterations that result from ligand-binding and conformational changes (Horn *et al*, 2006, Chalmers *et al*, 2011). Increased protection from solvent exchange (i.e., less solvent exchange) in localized regions of a protein indicates alterations in amide hydrogen bond networks and suggests that this region has been stabilized (directly or indirectly) by ligand binding and is thus less dynamic. Conversely, deprotection (i.e., increased solvent exchange) indicates that regional hydrogen bond networks have been disrupted, indicating that this protein region has become more dynamic or flexible. For our studies, conditions were optimized to obtain 75–80% sequence coverage. Most of the missing peptides corresponded to the PRD; hence, coverage of the remaining molecule was > 92%.

To identify conformational changes associated with nucleotide-binding and/or membrane interactions, we compared the amide deuterium exchange behavior in $Dyn1^{WT}$ tetramers alone (apo) or under 4 conditions: in solution bound to (i) the non-hydrolyzable GTP analogue, GMPPCP (β-γ-methyleneguanosine 5′-triphosphate) or (ii) the transition-state analogue, GDP•AlF_4^-, or assembled into helical scaffolds on PtdIns(4,5)P_2-containing lipid nanotubes in the (iii) absence or (iv) presence of GMPPCP. For interpretation, results from the HDX-MS experiments were mapped onto existing crystallographic and cryo-EM structures of dynamin (Chappie *et al*, 2011; Faelber *et al*, 2011; Ford *et al*, 2011; Sundborger *et al*, 2014; Reubold *et al*, 2015) (Fig 1B–E). Heat maps (Fig 1) show the extent of protection (slower exchange) or deprotection (increased exchange) relative to apo Dyn1.

We first analyzed nucleotide-dependent conformational changes occurring for $Dyn1^{WT}$ in solution. Mapping individual peptides whose HDX kinetics changed in the presence of GMPPCP (Figs 1B and 2A and C; Appendix Fig S1) or GDP•AlF_4^- (Figs 1C and 2C; Appendix Fig S2) relative to Dyn1WT-apo onto the $Dyn1^{WT}$ structure revealed nucleotide-binding sites and conformational alterations consistent with those observed in the minimal G domain-BSE structure (Chappie *et al*, 2010, 2011). Specifically, as expected for the GMPPCP-dependent swing of the BSE away from the G domain, we observed coordinated deprotection of the BSE in the presence of GMPPCP, as evidenced by changes in peptic peptides derived from the N- and C-terminus of the G domain ($BSE^{G,\ N\text{-}term}$, aa 10–20 and $BSE^{G,\ C\text{-}term}$, aa 280–313, respectively), as well as the C-terminus of GED (BSE^{GED}, aa 730–739) (Fig 2A and C) (Chappie *et al*, 2011; Mattila *et al*, 2015). We also observed increased protection to solvent exchange within the catalytic site of the G domain, especially in peptides derived from the P-loop (aa 38–48) and the G4 nucleotide interacting motif (aa 205–210), indicative of direct nucleotide binding. While peptides derived from the switch I region (aa 60–70) were not detected based on the stringent criteria used here, statistically significant changes in solvent exchange were observed in the switch II element (aa 136–153) and its associated *cis*-stabilizing loop (aa 108–120). Two peptides derived from within the G domain (aa 74–85 and 125–134) demonstrated increased solvent exchange upon GMPPCP binding. These regions, which lie between switch I and II and in the GED/GTPase domain interface, may play a role in transmitting changes in nucleotide binding to the BSE.

© 2016 The Authors

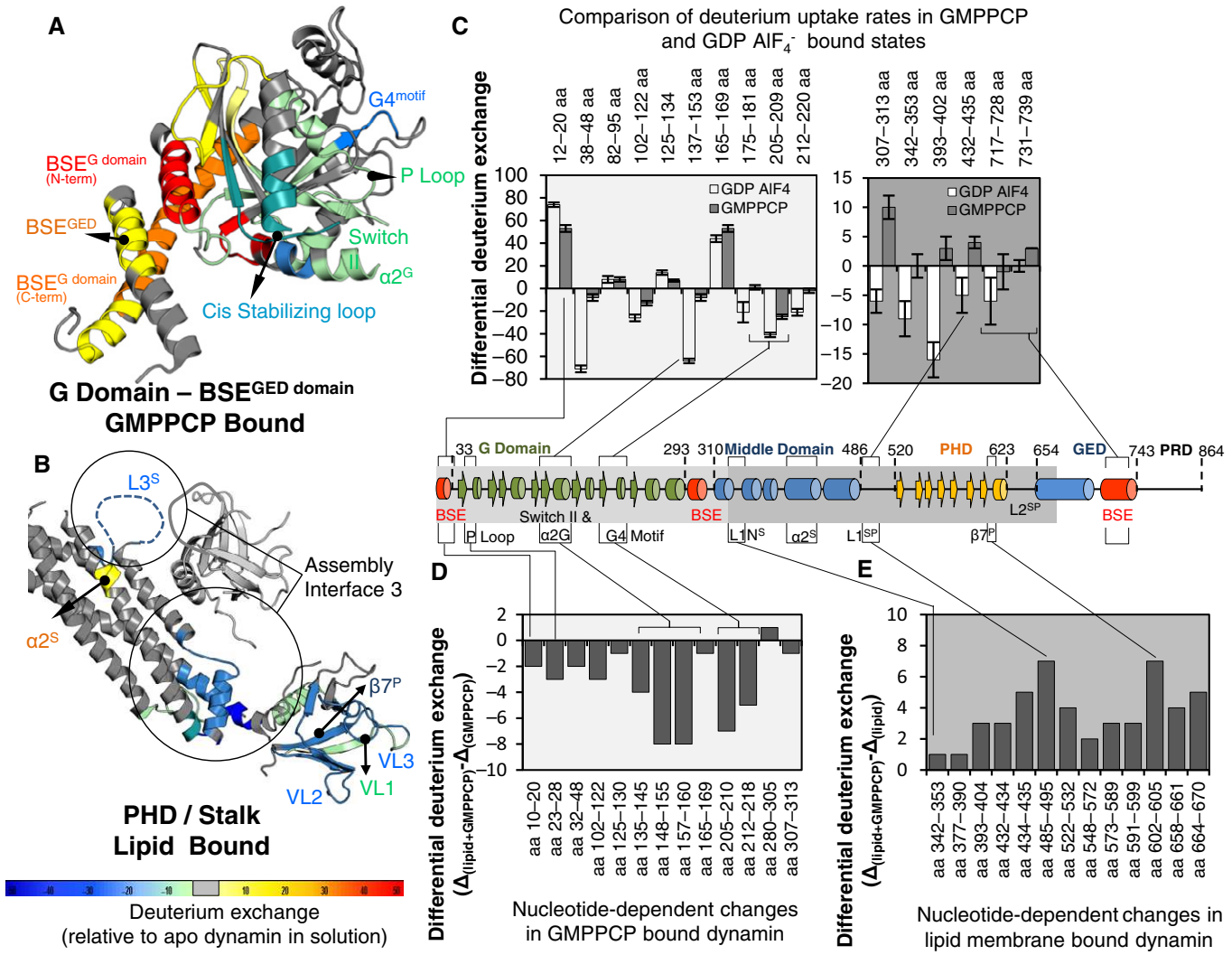

Figure 2. Differences in HDX behavior detected upon nucleotide and/or membrane binding.

A, B Changes in solvent exchange superimposed onto the structure (PDB ID: 2SNH) of the G domain (A) or the stalk/PHD of dynamin (B) in the GMPPCP- or lipid-bound states, respectively. Key structural elements are identified and the color coding shows the magnitude of solvent exchange relative to the apo state (see scale below).

C–E (C) Differential kinetics of solvent exchange of selected peptides that were identified as altered in both GMPPCP- and GDP•AlF_4^--bound states. The peptides are mapped to secondary structure elements on the polypeptide sequence. Differences in kinetics of solvent exchange of select peptides measured (n = 3, mean ± SEM) (D) for dynamin bound to GMPPCP in the presence or absence of lipid nanotubes and (E) for dynamin bound to lipid nanotubes in the presence or absence of GMPPCP.

Data information: HDX data are presented as means ± SEM of three independent triplicates and color coding is as in Fig 1. Paired two-tailed Student's t-test was performed to determine if the changes are statistically significant.

In the GDP•AlF_4^--bound state, the BSE is much less solvent-exposed relative to the GMPPCP-bound state, consistent with repositioning of the BSE against the G domain (Figs 1C and 2C; Appendix Fig S2). In addition to changes in the active site consistent with nucleotide binding, we also detect enhanced protection of switch II (aa 136–153) and G4-motifs (aa 205–210), known to be involved in GDP•AlF_4^--dependent G domain dimerization (Chappie *et al*, 2010). Together, these data provide compelling evidence that HDX can detect site-specific conformational changes in $Dyn1^{WT}$ associated with nucleotide binding.

Nucleotide-dependent conformational changes in the BSE are thought to be propagated along the structure to affect dynamin–assembly and dynamin–membrane interactions (Chappie *et al*, 2009, 2011; Mattila *et al*, 2015). However, the structural details of these conformational transmissions remained unknown. Therefore, we looked for any changes in the stalk and/or PHD that might reflect more global effects upon GMPPCP or GDP•AlF_4^- binding (Fig 1B and C). In the presence of GMPPCP, perturbation in solvent exchange was only detected in one region of the protein, corresponding to deprotection of residues 432–435 in the $\alpha2^S$ helix of the middle domain (Fig 2C). In contrast, in the presence of GDP•AlF_4^-, this same region showed increased protection, relative to apo, indicating that its conformation is sensitive to the nucleotide-bound state of the G domain. Interestingly, this region corresponds to a splice variant

 © 2016 The Authors

that occurs in both Dyn1 and Dyn2 (Cao *et al*, 1998). Within the tetramer, the C-terminus of the $\alpha2^S$ helix closely approaches the BSE of a neighboring dimer (Reubold *et al*, 2015) and hence may be positioned to transmit changes in BSE conformation to the stalk, especially in the assembled state. The obligate oligomeric nature of dynamin and the position of the relay helix at the oligomeric interface suggest that it is the core component of an intermolecular network that allows conformational transmission across seemingly autonomous domains. In addition, upon GDP•AlF_4^- binding, two long-range conformational changes were observed at the base of the stalk. These regions, $L1N^S$ (aa 342–353) and $L2^S$ (aa 393–402), correspond to interface 3, which is involved in higher-order dynamin assembly. The observed alterations in site-specific solvent exchange are consistent with the known ability of GDP•AlF_4^- to induced $Dyn1^{WT}$ higher-order assembly (Carr & Hinshaw, 1997) and provide direct evidence for transmission of nucleotide-dependent conformation changes from the G domain, through the BSE to the stalk.

HDX reveals nucleotide-dependent conformational changes in membrane-bound dynamin

Next, we mapped conformational changes induced upon dynamin assembly into a helical scaffold on PtdIns(4,5)P_2-containing lipid nanotubes. Consistent with recent data suggesting that the PHD can adopt multiple conformations in solution (Reubold *et al*, 2015), but then interacts stably with the lipid bilayer upon assembly, we detected an overall increased protection of the PHD upon membrane binding (Figs 1D and 2B). Particularly strong protection to solvent exchange was observed for all three VLs, which are believed to anchor dynamin onto the highly curved lipid nanotubes (Fig 2B, Appendix Fig S3). We also observed extensive increased protection in regions of the protein predicted to contribute to interface 3, which mediates higher-order assembly (Reubold *et al*, 2015). These include loop $L1N^S$ (aa 342–352), which is disordered in dynamin dimers and stabilized only upon higher-order dimer–dimer interactions (Reubold *et al*, 2015), loop $L2^S$ (aa 391–409), which encodes R399 a residue essential for higher-order oligomerization (Ramachandran *et al*, 2007) and helix $\alpha4^S$ (aa 657–670). As expected, the solvent exchange behavior in the highly conserved dimer interface 2 (aa 670–688) that encompasses the center of the criss-crossed stalks of two dynamin subunits and encloses a large buried surface area (Srinivasan *et al*, 2014; Reubold *et al*, 2015), remained unchanged upon higher-order assembly, although sequence coverage in this region was incomplete. Similarly, the solvent exchange behavior of the relatively small and potentially dynamic interface 1 (aa 320–330 & 685–695) remained unaltered between solution and membrane-bound states. Thus, as predicted by current models for scaffold assembly based on the tetrameric subunits (Reubold *et al*, 2015), the dimeric interface remains stable and relatively unchanged and higher-order scaffolding appears to be mediated predominantly by interface 3 (Fig 1D, Appendix Fig S3).

Interestingly, we also observed deprotection of regions containing residues 432–435 in the $\alpha2^S$ helix, the same region that exhibited nucleotide-dependent conformational changes (Fig 1B–D, inset). This conformational change appears to be triggered by either nucleotide binding or membrane binding, suggesting that the $\alpha2^S$ helix may play a role in relaying conformational information between the G domain and the membrane-interacting PHD.

We next examined HDX behavior for membrane-bound $Dyn1^{WT}$ in the presence of GMPPCP. Most of the changes observed were additive, reflecting a combination of GMPPCP and membrane-dependent conformational changes (Fig 1E, Appendix Fig S4). However, we note some quantitative differences. Specifically, residues that lie at the interface between G-G dimers that form between adjacent rungs (Chappie *et al*, 2010, 2011), including the G4 loop (aa 205–210), switch II (aa 136–153), and P-loop (aa 30–50), show increased protection compared to that observed for GMPPCP binding in solution (Fig 2D), likely reflecting increased G-G interactions. The two structural elements that were most sensitive to GMPPCP in the membrane-bound state were the flexible loop, $L4^S$ (aa 485–495), which connects the stalk to the PHD, and the VL3 of the PHD (aa 602–605) (Fig 2E). These regions exhibited protection with lipid alone, but were deprotected in the presence of GMPPCP, indicative of nucleotide-dependent changes in PHD–membrane interactions and GMPPCP-dependent loosening of the scaffold. We also detected increased protection to solvent exchange at the base of GED (aa 658–670), again indicative of long-range nucleotide-dependent conformational changes within membrane-bound dynamin. Given that few changes were observed along the 4-helical bundle of the stalk of membrane-bound dynamin upon GMPPCP binding, we concluded that these regions move as rigid bodies within the assembled structure to account for the conformational changes detected by cryo-EM in comparing nucleotide-free and GMPPCP-bound structures (Chen *et al*, 2004; Mears *et al*, 2007).

Combined, these data suggest a role for the $\alpha2^S$ helix, located within a splice variant, as a conformational sensor/relay. Thus, this region was particularly sensitive to nucleotide and/or membrane binding. The magnitude of deprotection (i.e., increased solvent exchange) for this region of dynamin under different conditions exhibited the following order: lipid nanotubes in the presence of GMPPCP > lipid nanotubes alone > GMPPCP in solution. In contrast, this region was protected from solvent exchange in the presence of GDP•AlF_4^-. This sensitivity provides further evidence for a role for the $\alpha2^S$ helix as an allosteric relay that facilitates conformational cross talk between the membrane-anchored PHD and the nucleotide-binding G domain.

PHD orientation serves as a conformation switch between cytosolic and membrane-bound states

Recent cryoEM (Sundborger *et al*, 2014) and crystal (Reubold *et al*, 2015) structures have provided strong evidence for conformational flexibility in the positioning of the PHD relative to the stalk and membrane. In its 'closed' conformation, the PHD is proposed to dock against the stalk. Transition to an 'open' conformation positions the PHD for membrane binding. We sought direct evidence for the conformational dynamics of the PHD through FRET (Förster resonance energy transfer) analysis. The PHD encodes four of the five tryptophan residues (Trp) in $Dyn1^{WT}$ (the fifth is located in the PRD) and thus offers a unique advantage as a chromophore-enriched region (Solomaha & Palfrey, 2005; Mehrotra *et al*, 2014). Strategic positioning of a FRET-based probe sensitive to these Trps should report the dynamic nature of the PHD. We chose 1,5-IAEDANS as the FRET sensor because of its compatibility with Trp emission (Trp: Ex = 295, Em = 340; IAEDANS: Ex = 337/

© 2016 The Authors

Em = 477) and sensitivity to close interactions (R_0 value of ~22 Å). Guided by the Dyn1 crystal structures (Faelber *et al*, 2011), we introduced a series of single cysteine mutants (H367C, I365C, S357C, Y354C, D352C) into a reactive cysteine-less Dyn1 construct (Ramachandran & Schmid, 2008) at the putative stalk-PHD interface for covalent modification with IAEDANS (Fig 3A). Of the five tested sites, maximal FRET efficiencies were observed upon labeling residues D352 and Y354 in the unstructured L1N^S loop (Fig 3B). Subsequent mutagenesis of the PHD Trps (to Phe) identified W525 and W542 as the major FRET donors (Fig 3C). Given the heterogeneity of PHD conformations observed in the crystal structures of Dyn3 tetramers (Reubold *et al*, 2015), the FRET intensities we measure for Dyn1 in solution likely represent the signal from a mixture of populations. This, together with the presence of multiple Trp donors, makes the measurement of exact FRET distances impossible; therefore, we report the relative FRET change between closed and open conformations. Nonetheless, these data are consistent with the recent structure of the Dyn3 tetramer (Reubold *et al*, 2015) and the positioning of at least some of the PHDs in the closed conformation.

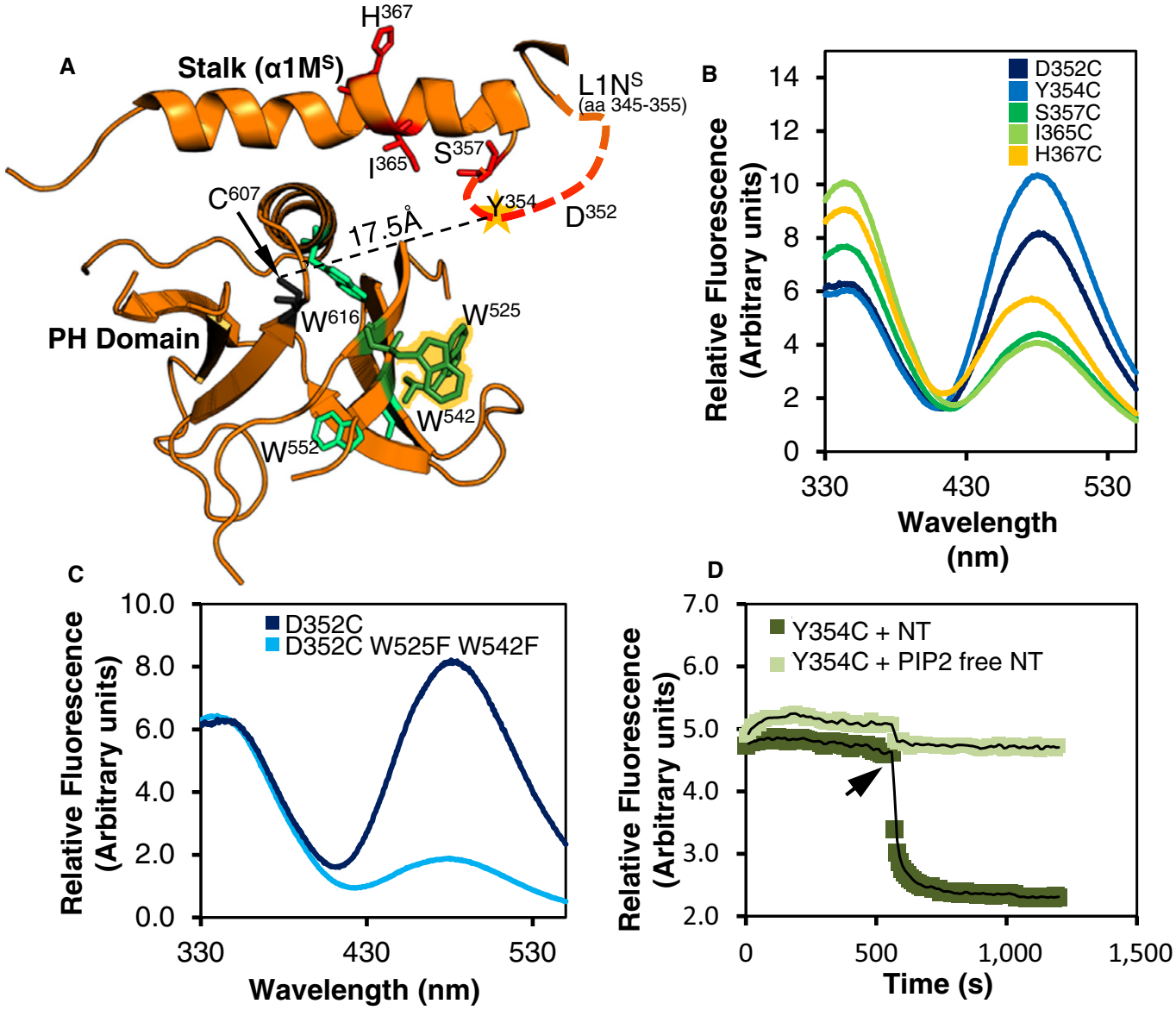

Figure 3. Large conformational changes of the PHD identified by FRET.

A Design of a functional dynamin mutant to probe PHD–stalk interactions. Minimal structure of the PHD and the PHD–stalk interface showing the location of important residues discussed in this study. The unresolved loop L1N^S in the stalk hosts the IAEDANS label and is sensitive to the two tryptophans (W525 and W542) in the PHD. The distance between two introduced cysteines (S357C and native C602) used to construct a double-cysteine Dyn1 is also shown.

B Comparison of emission spectra of various IAEDANS-labeled Dyn1 RCL variants (D352C, Y354C, S357C, I365C, H367C), upon Trp excitation at 295 nm.

C FRET transfer upon excitation is contributed by two neighboring Trps (W525 and W542); substitution by Phe resulted in significant loss of FRET.

D IAEDANS emission kinetics upon addition of lipid nanotubes with or without PI(4,5)P_2 (Ex = 295). The arrow indicates addition of lipids.

© 2016 The Authors

Although $Dyn1^{D352C}$ was functionally impaired, $Dyn1^{Y354C}$ exhibited near WT biochemical properties, whether or not it was conjugated with the IAEDANS fluorophore (Fig EV2A). Therefore, this mutant was subsequently used to test PHD–stalk dynamics. The efficient FRET transfer from the PHD to the stalk observed for $Dyn1^{Y354C\text{-}IAEDANS}$ in solution was rapidly lost upon binding to PtdIns(4,5)P_2-containing lipid nanotubes (Figs 3D and EV2B). The loss of FRET coincided with $Dyn1^{WT}$–membrane interactions as it was dependent on PtdIns(4,5)P_2, exhibited the previously described curvature sensitivity of $Dyn1^{WT}$ (Fig EV2C) (Liu *et al*, 2011; Mehrotra *et al*, 2014), and correlated with $Dyn1^{WT}$ membrane binding as measured by a sedimentation assay (Fig EV2D). To ensure that changes in the bulk FRET signal were not merely a reflection of dynamin oligomerization, we also measured FRET after dilution of dynamin into low salt buffers (Fig EV2E). Under these conditions, although dynamin oligomerizes, as reflected by a large increase in light scattering (inset Fig EV2F), we detected no changes in bulk FRET. Thus, the nearly twofold decrease in FRET-dependent IAEDANS emission upon membrane binding indicates that the PHDs undergo a large change in conformation consistent with movement away from the stalk and a transition from the closed to an open state.

Conformational flexibility of PHD underlies membrane binding and oligomerization

When in the closed conformation, the PHD is not positioned for membrane interaction; moreover, it obstructs assembly interface 3. Thus, the PHD has been proposed to play an auto-inhibitory role that regulates dynamin assembly and membrane interactions (Reubold *et al*, 2015). To test this hypothesis, we used two different strategies to trap the PHD in either its closed or open conformations (Fig 4A). For the former, we introduced a second cysteine into the PHD of $Dyn1^{Y354C}$ to enable intramolecular cross-linking of the PHD to the stalk. A series of cysteine replacements failed to exhibit WT-like activity consistent with the importance of the PHD in regulating dynamin assembly properties in solution. We subsequently designed a functionally unaltered double-cysteine variant by reintroducing the native cysteine at position 607, earlier altered to generate $Dyn1^{RCL}$. In the crystal structure, the distance between C607 and Y354 is ~18 Å (Fig 3A); however, this construct was efficiently cross-linked using the small ~7 Å disulfide cross-linker, MTS-2 (1,2-ethanediyl bismethanethiosulfonate) (Fig 4B, inset) consistent with molecular dynamic simulations of the PHD's ability to shift positions along the stalk (Reubold *et al*, 2015). Hereafter, we refer to cross-linked C354-C607 protein as $Dyn1^{Closed}$. To trap the PHD in its open, extended conformation, we truncated the two flexible loops connecting the PHD to the stalk (Fig 4A) by deleting residues 506–517 in $L1^{SP}$, which connects the PHD to the middle domain, and residues 635–649 in $L2^{SP}$, which connects the PHD to GED. The PHD in this construct, referred to as Dyn1ΔΔ, should be restrained in its open conformation at the base of the stalk.

As expected, $Dyn1^{Closed}$ failed to bind to lipid templates when analyzed for membrane binding by a sedimentation assay (Fig 4B inset) and consequently failed to exhibit any lipid NT/assembly-stimulated GTPase activity (Fig 4B). Moreover, $Dyn1^{Closed}$ was unable to catalyze membrane fission and the release of vesicles from SUPER templates (Fig 4C). However, all of these activities were rescued upon addition of sufficient reducing agent to reverse the cross-link, indicating that the defect was not due to covalent modification by the cross-linker. At room temperature, $Dyn1^{Closed}$ eluted as a dimer upon size-exclusion chromatography (Fig 4D), establishing that locking the PHDs in the closed conformation indeed prevents tetramerization of $Dyn1^{WT}$. However, G domain interactions can still occur, as $Dyn1^{Closed}$ forms higher-order oligomers in the presence of GDP•AlF_4^- (Fig EV3A). At higher temperatures, we detected aggregates that eluted in the void volume (Fig 4D) and appeared amorphous by negative-stain EM (Fig EV3B). Consistent with this, $Dyn1^{Closed}$ exhibited higher basal GTPase activity, when measured at 37°C, compared to the control (Fig 4B), which was concentration-dependent even in the low μM range (Fig EV3C).

Although Dyn1ΔΔ was well expressed, it had diminished yield owing to aggregation during purification. Indeed, in contrast to $Dyn1^{Closed}$, which eluted upon gel filtration as a dimer, soluble Dyn1ΔΔ eluted as tetramers and higher-order oligomers (Fig 4E). Also in contrast to $Dyn1^{Closed}$, Dyn1ΔΔ was able to bind to lipid nanotubes, although the helical scaffold packing appeared to be more compressed (i.e., shorter pitch) and irregular when compared to $Dyn1^{WT}$ (Fig 4F). In addition, we observed abundant ring-like structures alongside the membrane tubules on Dyn1ΔΔ grids, not observed with $Dyn1^{WT}$ (Fig EV3D). The assembly-stimulated GTPase activity of Dyn1ΔΔ on NT was diminished (Fig 4G); however, Dyn1ΔΔ no longer showed the curvature sensitivity exhibited by $Dyn1^{WT}$. Indeed on liposomes > 400 nm in diameter, Dyn1ΔΔ exhibited assembly-stimulated GTPase activity comparable to $Dyn1^{WT}$. Remarkably, Dyn1ΔΔ also retained WT-like ability to catalyze membrane fission and vesicle release from SUPER templates (Fig 4H). While these data support the idea that in its open conformation, $Dyn1^{WT}$ is capable of self-assembly, membrane interactions, and fission, they also suggest that PHD conformational flexibility is important to ensure that dynamin self-assembly into higher-order oligomers occurs only after membrane binding.

Together with the FRET studies described above, the properties of dynamin trapped in the 'open' or 'closed' conformations provide direct evidence that the PHD of dynamin in solution exists in equilibrium between open and closed conformations and that this conformational switch is required to regulate dynamin tetramerization and higher-order assembly.

A common disease-causing mutation, S619L, affects the PHD conformational switch

Mutations in ubiquitously expressed Dyn2 are linked to centronuclear myopathy (CNM) and Charcot–Marie–Tooth peripheral neuropathy (Durieux *et al*, 2010). Interestingly, the majority of these mutations map to the PHD or the stalk (Faelber *et al*, 2011), including S619L, a common and severe CNM-causing mutation. Previous *in vitro* studies have shown that $Dyn1^{S619L}$ exhibits increased oligomerization and basal GTPase activity (Kenniston & Lemmon, 2010). Interestingly, like $Dyn1^{WT}$, $Dyn2^{S619L}$ eluted as a tetramer upon gel filtration at 22°C, but formed higher-order oligomers that eluted in the void volume at 37°C (Fig EV4A, see also Kenniston & Lemmon, 2010). Negative-stain EM show increased abundance of aggregated protein at 37°C, when compared to the protein equilibrated at room temperature (Fig EV4C). Consistent

© 2016 The Authors

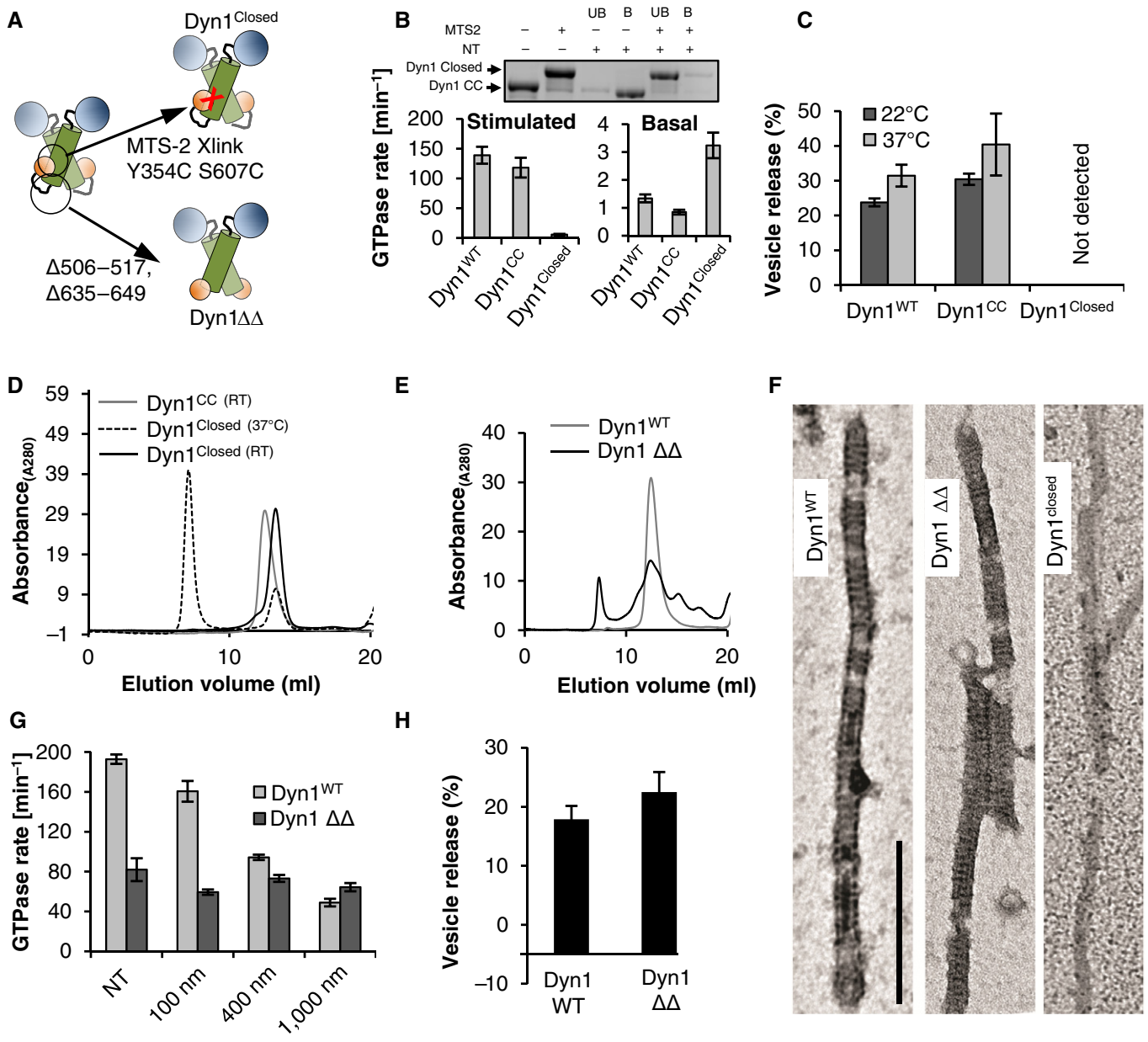

Figure 4. Biochemical properties of PHD 'closed' and 'open' states.

A Design of dynamin mutants to restrict the PHD in the closed ($Dyn1^{Closed}$) or open (Dyn1ΔΔ) state.

B Histogram shows basal and assembly-stimulated GTPase activities of non-cross-linked $Dyn1^{CC}$ versus cross-linked $Dyn1^{Closed}$ and $Dyn1^{WT}$. Inset shows cross-linking of the PHD and stalk domains in $Dyn1^{Y354C/S607C}$ ($Dyn1^{CC}$) with the bifunctional cross-linker, MTS-2-MTS, to yield $Dyn1^{Closed}$, which migrates more slowly on SDS–PAGE, as well as liposome binding of $Dyn1^{CC}$ compared to $Dyn1^{Closed}$ (bound, B; unbound, UB).

C Ability of $Dyn1^{WT}$, $Dyn1^{CC}$, and $Dyn1^{Closed}$ to catalyze membrane fission and vesicle release from SUPER templates.

D Size-exclusion chromatographic profiles of $Dyn1^{CC}$, $Dyn1^{Closed}$ at room temperature or after incubation for 10 min at 37°C.

E Oligomeric state of Dyn1ΔΔ at room temperature.

F Negative-stain electron micrographs of $Dyn1^{WT}$, Dyn1ΔΔ, and $Dyn1^{Closed}$ assembled onto lipid nanotubes. Scale bar, 200 nm.

G Curvature-dependent liposome-stimulated GTPase activity of $Dyn1^{WT}$ and Dyn1ΔΔ.

H Ability of $Dyn1^{WT}$ and Dyn1ΔΔ to catalyze membrane fission and vesicle release from SUPER templates.

Data information: GTPase activity and vesicle fission assays represent mean ± SEM from 3 independent experiments.

with the temperature-sensitive oligomerization of $Dyn2^{S619L}$, its assembly-stimulated GTPase activity and NT binding (Figs 5A and EV4B) were comparable to $Dyn1^{WT}$ at 22°C, but severely impaired at 37°C. Basal activity also increased (Fig 5A), presumably due to dysregulated self-assembly at elevated temperatures. Surprisingly, when measured at 22°C, $Dyn2^{S619L}$ exhibited significantly enhanced fission activity compared to $Dyn2^{WT}$, consistent with a gain-of-function mutation (Fig 5B, see also Chin *et al*, 2015). However,

 © 2016 The Authors

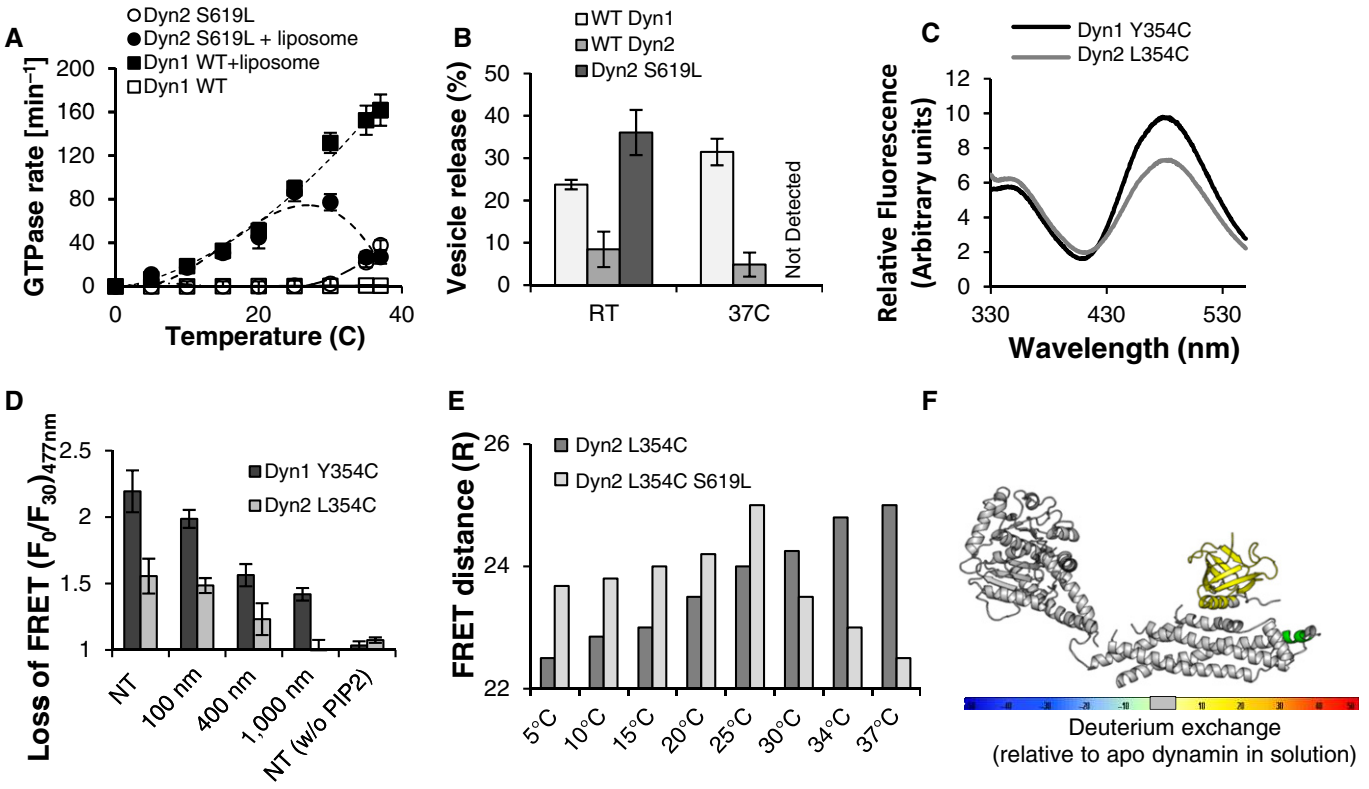

Figure 5. Biochemical properties and PHD conformational dynamics of Dyn2, disease-associated S619L mutant.

A Temperature dependence of basal and lipid-stimulated GTPase activity of $Dyn1^{WT}$ and $Dyn2^{S619L}$.

B Temperature-sensitive membrane fission activity of $Dyn1^{WT}$, $Dyn2^{WT}$, and $Dyn2^{S619L}$ measured using SUPER templates.

C Detection of Dyn2 PHD–stalk interactions by FRET using IAEDANS-labeled $Dyn2^{L354C}$.

D Curvature-dependent membrane binding and consequent opening of PHD in $Dyn1^{Y354C\text{-}IAEDANS}$ and $Dyn2^{L354C\text{-}IAEDANS}$.

E Differential temperature dependence of PHD–stalk FRET for WT and S619L mutant $Dyn2^{IAEDANS}$. Data are presented as relative FRET distances assuming a single donor/acceptor pair.

F Differential solvent exchange kinetics of $Dyn1^{S619L}$ at ambient temperature compared to $Dyn1^{WT}$ under identical conditions. Yellow coloring indicates a significant increase in HDX. Quantitative data on the individual peptides used to generate this map are provided in Appendix Fig S5.

Data information: The GTPase activity, vesicle fission and membrane binding-dependent FRET loss assays represent means ± SEM from 3 independent experiments.

fission activity was also severely impaired when assayed at 37°C (Fig 5B).

We hypothesize that the temperature-sensitive phenotype of the $Dyn1^{S619L}$ mutant reflected temperature-sensitive changes in the steady-state conformation(s) adopted by the PHD. To test this, we introduced the S619L mutation into a single cysteine variant of $Dyn2^{WT}$, to generate $Dyn2^{L354C}$ for IAEDANS labeling and FRET measurements (the Trp residues are conserved in the Dyn2 PHD). In the absence of the disease mutation, and like $Dyn1^{WT}$, efficient FRET was detected between the stalk-conjugated IAEDANS and the PHD-localized Trp residues in $Dyn2^{WT}$ (Fig 5C). Also, like $Dyn1^{WT}$, upon membrane binding the FRET signal decreased (Fig 5D), consistent with a shift of the PHD toward the open conformation. As previously shown, $Dyn2^{WT}$ exhibited greater curvature dependence for membrane binding than $Dyn1^{WT}$ and failed to bind liposomes > 1,000 nm in diameter (Fig 5D). Moreover, the degree of FRET loss upon binding to highly curved membranes was lower for $Dyn2^{WT}$ than $Dyn1^{WT}$, consistent with weaker interactions of the Dyn2 PHD with the membrane as compared to $Dyn1^{WT}$ (Liu *et al*, 2011).

We next compared the effect of temperature on PHD–stalk interactions by measuring relative FRET distances (assuming a single donor/acceptor system) for both WT and S619L $Dyn2^{IAEDANS}$ in solution. The relative FRET distance measured for $Dyn2^{WT\text{-}IAEDANS}$ was minimal at 5°C but then markedly increased with increasing temperature, presumably reflecting temperature-dependent increased mobility of the PHD away from the stalk as it fluctuates between open and closed states (Fig 5E). Like $Dyn2^{WT\text{-}IAEDANS}$, $Dyn2^{S619L\text{-}IAEDANS}$ also exhibited a temperature-dependent increase in relative FRET distances between 5°C and 25°C. However, at these temperatures, the relative FRET distances between the PHD and stalk were greater in the $Dyn2^{S619L\text{-}IAEDANS}$ compared to $Dyn2^{WT\text{-}IAEDANS}$ (Fig 5E), consistent either with a shift toward a more open conformation and/or greater mobility of the PHD between open and closed states. This increase mobility of the PHD was also evident in HDX measurements performed at room temperature, which showed increased solvent exchange throughout the PHD (Fig 5F, Appendix Fig S5). Given the enhanced fission activity of $Dyn2^{S619L}$ relative to $Dyn2^{WT}$ at room temperature, these data further support the hypothesis that the closed conformation of the PHD negatively

© 2016 The Authors

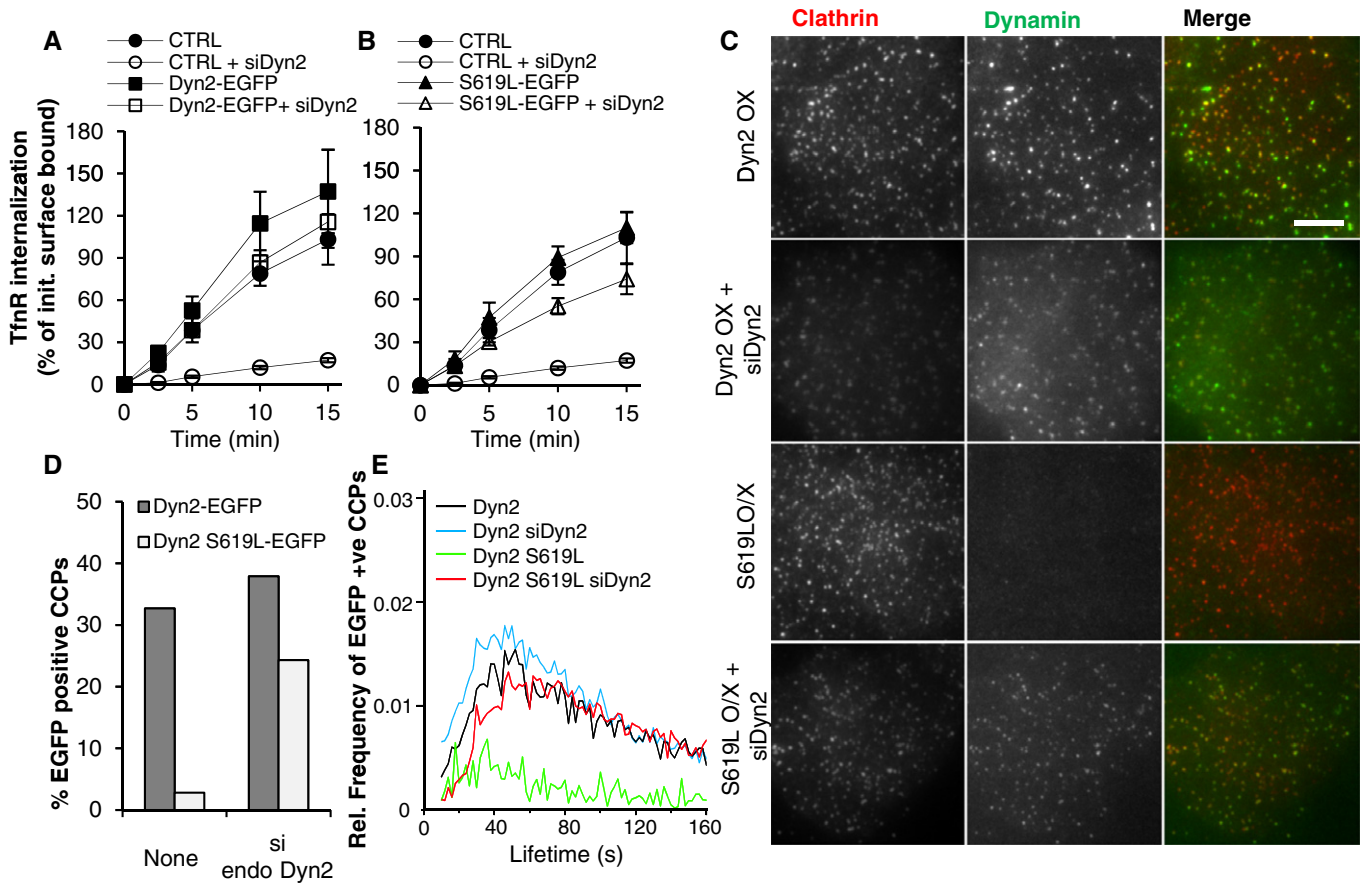

Figure 6. ***In vivo*** **function of CNM-causing Dyn2 mutant S619L.**

A, B Transferrin receptor (TfnR) uptake, a measure of CME, shown as % uptake of total initial surface TfnR for control H1299 cells, and H1299 cells stably expressing low amounts of siRNA-resistant $Dyn2^{WT}$-EGFP (A) or $Dyn2^{S619L}$-EGFP (B) with or without treatment with siRNA directed toward endogenous Dyn2.

C Fixed cell TIRF-M images of $Dyn2^{WT}$-EGFP- or $Dyn2^{S619L}$-EGFP-expressing H1299 cells with or without Dyn2-siRNA treatment showing co-localization of dynamin with clathrin light chain immunostained with rabbit anti-CLC and Alexa 547-conjugated secondary antibodies. Scale bar, 5 μm.

D Percentage of Dyn2-EGFP-positive clathrin-coated pits detected by live cell TIRF-M and automated master/slave image analysis (Aguet *et al*, 2013).

E Lifetime analysis of CCPs which are positive for EGFP-$Dyn2^{WT}$ or EGFP-$Dyn2^{S619L}$ with or without siRNA-mediated specific knockdown of endogenous Dyn2.

Data information: TfnR uptake assays represent means ± SEM from 4 independent experiments. Relative frequency and percentage of EGFP-positive CCPs were obtained by analyzing > 60,000 individual CCPs per condition.

regulates dynamin function (Fig 5B). In striking contrast to $Dyn2^{WT}$, at temperatures higher than 25°C, we observed a precipitous decrease in PHD–stalk FRET distance in $Dyn2^{S619L\text{-}IAEDANS}$. While this could reflect a shift of the PHD toward the closed state, the interpretation of this change in FRET signal is complicated by the fact that $Dyn2^{S619L}$ assembles/aggregates at these elevated temperatures (Fig EV5A and D; Chin *et al*, 2015; Kenniston & Lemmon, 2010). Indeed, the higher-order structures formed by $Dyn2^{S619L}$ at these elevated temperatures likely reflect dysregulated assembly, because rather than rings or spirals, we observe amorphous aggregates by negative-stain EM, only at 37°C (Fig EV5D). We interpret the increased FRET efficiency (decreased FRET distance) observed for $Dyn2^{S619L\text{-}IAEDANS}$ at 37°C to have resulted from constraint of the PHDs between molecules in $Dyn2^{S619L}$ aggregates. Overall, our FRET data suggest that the S619L mutation destabilizes PHD–stalk interactions leading to increased flexibility of the PHD that results in reduced auto-inhibition at lower temperatures, but dysregulated and aberrant dynamin assembly at physiological temperatures.

In vivo function of Dyn2 S619L

Centronuclear myopathy (CNM) patients are heterozygous for disease mutations of Dyn2. To test for $Dyn2^{S619L}$ function *in vivo*, we generated ARPE19 cells stably overexpressing $Dyn2^{WT}$-EGFP or $Dyn2^{S619L}$-EGFP tagged proteins and FACS-sorted for low levels of overexpression. Even at these low levels (~twofold over controls, Fig EV5A), we observed large aggregates of $Dyn2^{S619L}$-EGFP (Fig EV5B) not detected in cells expressing comparable levels of $Dyn2^{WT}$-EGFP. These data are consistent with the dysregulated assembly we observed *in vitro* at 37°C. In an effort to obtain stable cells expressing lower levels of $Dyn2^{WT}$ and mutant, we switched to H1299 non-small cell lung cancer cells and were able to select cells that stably expressed very low levels of $Dyn2^{WT}$-EGFP or $Dyn2^{S619L}$-EGFP fusion proteins (~50% of endogenous), neither of which formed detectable aggregates. Control experiments established that $Dyn2^{WT}$-EGFP was fully functional and could restore CME of transferrin receptor (TfnR) to control levels upon specific

 © 2016 The Authors

knockdown of endogenous Dyn2 by siRNA (Fig 6A). In the presence of endogenous Dyn2, we detect no change in the rate of CME in cells expressing $Dyn2^{S619L}$-EGFP (Fig 6B). Unexpectedly, given the severe defects in Dyn^{S619L} activity measured *in vitro* at 37°C, and its lower levels of expression, this mutant was able to restore CME to ~70% of control levels even in the absence of endogenous $Dyn2^{WT}$ (Fig 6B). Consistent with these findings, it has been shown that overexpression of $Dyn2^{S619L}$ in myoblasts leads to T tubule fragmentation, but does not impair endocytosis (Chin *et al*, 2015).

Exploring the activity of $Dyn2^{S619L}$-EGFP further, we found that in the presence of endogenous Dyn2, the mutant was not efficiently recruited to the plasma membrane, as assessed by total internal reflection fluorescence microscopy (TIRF-M) (Fig 6C). In contrast, upon siRNA knockdown of endogenous Dyn2, the mutant $Dyn2^{S619L}$-EGFP could be recruited to clathrin-coated pits (CCPs) (Fig 6D), where it partially functioned to restore CME. From this, we conclude that endogenous Dyn2 competes more effectively for membrane-binding sites than the S619L mutant. In the absence of competition from the endogenous, the mutant is recruited. This interpretation is supported by *in vitro* biochemical data with purified proteins (Fig EV4B), where WT-Dyn2 binds liposomes more effectively than S619L. Other factors, including impaired binding to partners responsible for membrane recruitment, could affect this competition.

We have previously shown that dynamin can regulate CCP maturation (Aguet *et al*, 2013) and that bulk, biochemical measurements of CME might not detect resulting alterations in CCP maturation kinetics (Reis *et al*, 2015). Therefore, we wondered whether the disease-causing S619L mutation might affect earlier stages in CCP maturation not evident by our bulk measurements of CME. Such changes would be evident in the lifetime distribution of CCPs measured by TIRF-M (Aguet *et al*, 2013; Reis *et al*, 2015). To test this idea, we infected $Dyn2^{WT}$-EGFP- and $Dyn2^{S619L}$-EGFP-expressing cells with adenoviruses encoding clathrin light chain-TdTomato as a fiduciary marker of CCPs. Using TIRF-M, automated detection and a master (TdTomato)-slave (EGFP) approach (Aguet *et al*, 2013), we measured the fraction and lifetimes of CCPs that co-localize (at any time during their lifetimes) with EGFP-labeled WT or S619L mutant Dyn2. Consistent with steady-state TIRF measurements (Fig 6C), we find a slight increase in the fraction of CCPs co-localizing with $Dyn2^{WT}$-EGFP following siRNA-mediated knockdown of endogenous Dyn2 (from 32.7 to 37.9%, respectively, Fig 6D), but a marked increase in recruitment of $Dyn2^{S619L}$-EGFP to CCPs following depletion of endogenous Dyn2 (from 2.8 to 24.3%, Fig 6D). Consistent with the ability of $Dyn2^{WT}$-EGFP to rescue TfnR CME in Dyn2 siRNA-treated cells, we detect no significant differences in the lifetime distribution of $Dyn2^{WT}$-positive CCPs in the presence (Fig 6E, black line) or absence (blue line) of endogenous Dyn2. Few CCPs are positive for $Dyn2^{S619L}$-EGFP in the presence of endogenous Dyn2 (green line). However, in the absence of endogenous Dyn2, the distribution is shifted toward longer lifetimes, but otherwise retains the shape of Dyn^{WT} and control cells. As Dyn2-positive CCPs are believed to represent productive endocytic events (Ehrlich *et al*, 2004; Taylor *et al*, 2012; Aguet *et al*, 2013), these data are consistent with the slightly slower kinetics of TfnR uptake observed in cells expressing only $Dyn2^{S619L}$ (Fig 6B), but otherwise unperturbed maturation. Given the contrast between the severe defects we observe for $Dyn2^{S619L}$ function *in vitro* at 37°C (Fig 5) and the rather modest defects in $Dyn2^{S619L}$-supported CME at 37°C *in vivo* (Fig 6), we speculate that other factors, presumably dynamin binding partners and/or protein chaperones, are activated to help control the PHD conformational switch enabling membrane targeting and activation of this mutant. Differences in these compensatory mechanisms may explain the tissue-specific and late onset disease phenotypes resulting from Dyn2 mutations.

Conclusions

The modular nature of dynamin allows for large conformational flexibility that is critical for its mechano-enzymatic activity (Schmid & Frolov, 2011; Chappie & Dyda, 2013). Although most conformational changes are locally restricted to the nucleotide, self-assembly, or membrane-binding domains, HDX revealed long-range conformational changes that are propagated from the G domain through the stalk to the membrane and vice versa. In particular, we identified C-terminal residues (aa 432–435) within the $\alpha2^S$ helix (aa 406–445) of the stalk as a region altered by nucleotide-binding and membrane interactions and the two in combination. In the crystal structure (Faelber *et al*, 2011), Arg440 forms an intermolecular salt bridge with Asp744 in the neighboring BSE. Thus, the $\alpha2^S$ helix may act as an allosteric relay to convey long-distance conformational changes between the G domain and the stalk to regulate dynamin function. Interestingly, this region corresponds to splice variants conserved in both Dyn1 and Dyn2 (Cao *et al*, 1998) and perturbation of this salt bridge in Dyn2 resulted in increased rates of transferrin uptake (Faelber *et al*, 2011). Interestingly, this region is also in close proximity to Arg465, which is mutated in several CNM patients. R465W is one of the few disease-causing mutations not confined to the PH or the PH–stalk interface (Durieux *et al*, 2010), confirming the importance of this region for dynamin function.

Dynamin-catalyzed fission requires GTP hydrolysis and presumably nucleotide-driven conformational changes that affect dynamin–dynamin and dynamin–membrane interactions. Thus, by HDX we observed significant nucleotide-dependent changes at interface 3 that governs higher-order dynamin assembly. This region became deprotected in the presence of GMPPCP, consistent with a GTP-dependent loosing of the scaffold, and showed increased protection in the presence GDP•AlF_4^-, consistent with the ability of this transition-state analogue to trigger assembly and constriction of the scaffold (Carr & Hinshaw, 1997; Sundborger *et al*, 2014). When trapped in its transition-state conformer by locking the BSE to the G domain and mimicking the GDP•AlF_4^--bound state, dynamin was unable to catalyze complete membrane fission; however, it was able to constrict membranes and generate stable hemi-fission intermediates, even in the absence of nucleotide, due in part to enhanced PHD–membrane interactions (Mattila *et al*, 2015). Consistent with these observations, our HDX analyses showed that GDP•AlF_4^- binding generated more, higher-magnitude, and longer-range conformational changes than GMPPCP binding (Fig 2C and compare Appendix Fig S2A and B). These data provide new insights into the nature of the nucleotide-driven, long-range conformational changes involved in dynamin-catalyzed membrane fission.

Here, we have used FRET measurements to confirm the conformational mobility in the PHD and demonstrate that in solution it

© 2016 The Authors

docks along the stalk in a closed conformation and opens upon membrane binding. By locking the PHD in either the 'closed' or 'open' conformation, we provide direct evidence for the importance of this conformational switch in regulating the tetramerization and higher-order assembly of dynamin, as well as its GTPase and fission activities *in vitro*. Our finding that the S619L mutant, which is severely impaired *in vitro*, can function to support CME *in vivo* suggests that other, extrinsic factors might also be able to regulate the PHD conformational switch.

The PHD is a highly abundant structural motif, originally identified to bind to phosphoinositides and serve as a membrane anchor. However, increasing evidence points to their role as regulatory domains of signaling GTPases and kinases through protein–protein interactions (Bellacosa *et al*, 1998; Lemmon, 2007; Scheffzek & Welti, 2012). Dynamin is targeted to CCPs, presumably as dimers or tetramers (Cocucci *et al*, 2014), via protein interactions between its PRD and SH3 domain-containing partners. Dyn2 is proposed to regulate early stages of CCP maturation and then, upon self-assembly around the necks of deeply invaginated CCPs, to catalyze membrane fission (Liu *et al*, 2011; Schmid & Frolov, 2011). Auto-inhibition by the PHD could serve to regulate either dynamin recruitment and/or this "assembly switch" that demarks early and late stages of CME.

Materials and Methods

Preparation of dynamin RCL mutants, protein expression, purification, and dynamin fluorescence labeling

Dynamin mutants carrying site-specific cysteine and Trp modifications were generated from a reactive cysteine-less mutant dynamin construct (Ramachandran & Schmid, 2008) using quikchange site-directed mutagenesis (Agilent). The cDNA were cloned in pIEx-6 insect cell expression vectors between NcoI and NotI sites. Dyn1, Dyn2 and their variants were all expressed by transient transfection in Sf9 insect cells and purified by affinity chromatography using GST fused Amphiphysin II SH3 domain, following previously described approach (Leonard *et al*, 2015). Purified dynamin proteins were stored in 20 mM HEPES, 150 mM KCl, and 2 mM $MgCl_2$. For long-term storage (−80°C), 10% glycerol was added to these preparations. Fluorescence labeling of the lone cysteine in RCL dynamin variants were performed by incubating the protein free of reducing agents into fold molar excess fluorescence probe IAEDANS (1,5-IAEDANS, [N-(Iodoacetaminoethyl)-1-naphthylamine-5-sulfonic acid]; I-14 Life Technologies) and extensively dialyzed at 4°C to excess dye. The labeling efficiency was determined using the molar absorptivity values of 58,790 M^{-1} cm^{-1} at 280 nm and 5,600 M^{-1} cm^{-1} at 337 nm for dynamin and 1,5-IAEDANS, respectively. Typically near equimolar labeling ratios were achieved.

GTPase activity and liposome-binding assays

GTPase activity of dynamin was determined using the previously described malachite green assay (Leonard *et al*, 2005). GTP was obtained as 100 mM stock solution (Jena Biosciences, Germany) and used as 1 mM in all assays unless specified. Protein concentrations were 0.5 μM dynamin. EAP concentrations were kept equimolar for all the assays in a buffer containing 20 mM HEPES pH 7.5, 150 mM KCl, 1 mM GTP, and 2 mM $MgCl_2$. For stimulated GTPase assay, the lipid concentration was ~200-fold excess.

For liposome preparation, lipid mixtures (DOPC:DOPS:PIP2 75:15:10 mol%) were dried for 2 h at 45°C in vacuum and rehydrated in buffer (20 mM HEPES, pH 7.5, and 150 mM KCl) to a final concentration of 1 mM. The hydrated liposomes were subjected to multiple cycles of freeze–thaw and extruded through polycarbonate membranes (Whatman, Clifton, NJ) of predefined pore size using Avanti Mini-Extruder. Lipid nanotubes were prepared using lipid mixture (DOPC:GalCer:PiP2 – 45:45:10 mol%), dried as described above and hydrated in 20 mM HEPES and 100 mM NaCl. The hydrated lipid was subjected to 2 min of sonication and brief vortexing and stored in low-adhesion microcentrifuge tubes (USA Scientific). The lipid preparations were stored at 4°C and used within 2 days of preparation.

Chemical cross-linking and SDS–PAGE analysis

Chemical cross-linking was performed with thiol-specific methanethiosulfonate (MTS) cross-linkers containing spacer arms of 2 to 17 atoms (Toronto Research Chemicals, Canada) as previously described (Srinivasan *et al*, 2014). Protein stocks containing reducing agents were first desalted with desalting columns (Zeba spin, Thermoscientific) and incubated with 10-fold excess cross-linker at room temperature for 2 min before quenching excess and unreacted cross-linker with 50-fold excess N-ethylmaleimide. The extent of cross-linking was analyzed using a 7.5% SDS–PAGE precast gel (Bio-Rad). Cross-linking was highly efficient and typically > 90%.

Size-exclusion chromatography

Dynamin mutants and cross-linked variants were analyzed on Superose 6 10/300 GL analytical grade size-exclusion column (GE Life Sciences, Piscataway, NJ) on an AKTA FPLC. The analytes were pre-incubated at appropriate temperatures and analyzed on the size-exclusion column equilibrated with 20 mM HEPES, 150 mM KCl, 2 mM $MgCl_2$, 1 mM EGTA, pH 7.5 at room temperature.

Fluorescence spectroscopy assays

Steady-state fluorescence measurements were performed with a Fluorolog 3-22 fluorometer (Horiba Jobin Yvon, Edison, NJ) equipped with a 450-W xenon lamp, a cooled PMT housing, and a temperature-controlled sample compartment. All measurements were performed at RT unless otherwise specified. FRET efficiency (E) was calculated using the equation $E = 1 - (F_{DA} - F_D)$, where F_{DA} is the emission intensity of Trp monitored at 330 nm in the presence of acceptor IAEDANS and F_D, the emission intensity in the absence of acceptors. The Förster radius R_0 is the characteristic distance for a FRET pair at which the efficiency of energy transfer (E) is 50%. Tryptophan was excited at 295 nm to minimize contribution of tyrosine emission, and the spectral scans were obtained from 330 to 550 nm. The excitation and emission slit were maintained at 4 nm, and the integration time was set to 0.1 s. The assay volume was 600 μl (0.1 μM dynamin concentration) and 60 μl (0.5 μM dynamin concentration) and assayed using microcuvettes from Hellma. The Trp fluorescence (λ_{ex} 295 nm and λ_{em} 340 nm) and IAEDANS

 © 2016 The Authors

absorption spectra (λ_{ex} 336 nm and λ_{em} 478 nm) overlap to allow efficient fluorescence energy transfer. The distance R between the donor and acceptor was calculated by the Förster equation

$$E_{FRET} = \left[1 + \left(\frac{R}{R_o}\right)^6\right]^{-1}$$

where the Förster radius R_0, distance for a FRET pair at which the efficiency of energy transfer (E) is 50%, is 22 Å for the Trp-IAEDANS FRET pair (Jeganathan *et al*, 2006).

Membrane fission and curvature generation

The ability of dynamin to generate curvature and cause fission was probed using the previously described SUPER template assay (Neumann *et al*, 2013). Briefly, silica beads (15×10^6 silicon oxide microspheres d = 2.5 μm Corpuscular, Cold Spring, NY) were incubated with 200 μmol of 100 nm extruded RhoPE-labeled liposomes (DOPG:DOPC:DOPS:PIP2:RhPE – 40:39:15:5:1 mol%) in 350 mM NaCl. The mix was incubated for 30 min at room temperature with intermittent shaking to ensure lipid–silica bead interaction. The templates were washed with filtered water through three rounds of centrifugation at 250 *g* and ~100 μl of water was retained after the final wash. The beads were gently tapped to ensure homogeneous mixture, stored in dark at room temperature, and used within 2–4 h of preparation.

Vesicle release from SUPER template was used to measure fission capability of dynamin. Dynamin was incubated in buffer containing 20 mM HEPES pH 7.5, 150 mM KCl, 1 mM $MgCl_2$, and 1 mM GTP at a final volume of 90 μl. To this, SUPER templates were added (~20×10^5 beads) to a final volume of 100 μl. Fission was allowed to proceed over 30 min at room temperature, and the templates were separated from released vesicles by pelleting the templates only at 260 *g* in a swing-out centrifuge rotor. The supernatant was assayed for its fluorescence in a 96-well fluorescent plate reader (Bio-Tek Instruments) with appropriate excitation and emission filters (for RhPE excitation = 530/25 nm bandwidth and emission = 580/25 nm bandwidth). Total fluorescence of templates was determined in a separate reaction containing the same amount of SUPER templates in 0.1% Triton X-100 in 20 mM HEPES pH 7.5, 150 mM KCl, and 1 mM $MgCl_2$. Fluorescence was measured in a microplate setup, and vesicle release is expressed as RhPE released into the supernatant as percentage of total RhPE fluorescence of SUPER templates. Fluorescence released in the absence of GTP is subtracted as background.

Sedimentation assay

Lipid-induced self-assembly of dynamin was analyzed by spin-centrifugation and SDS–PAGE gel analysis of fraction pelleted versus supernatant as previously described (Ramachandran *et al*, 2007). Dynamin mutants and wild-type proteins were pre-incubated with appropriate lipid nanotubes and liposomes of varying curvatures for 30 min at room temperature. The reaction mixtures were spun at 20,800 *g* for 20 min in a table-top microcentrifuge. The supernatant (unbound, UB) and pellet (bound, B) were separated and analyzed on a 7.5% PAGE gel. The fraction bound/unbound were calculated based on gel band intensity quantification.

Hydrogen–deuterium exchange mass spectrometry

Solution-phase amide HDX experiments were carried out with a fully automated system (CTC HTS PAL, LEAP Technologies, Carrboro, NC; housed inside a 4°C cabinet) as described previously (Chalmers *et al*, 2006) with slight modifications. Dynamin (10 μM) in the absence or presence of lipid nanotubes (1 mM lipid final), nucleotides (1 mM final), or their combinations was incubated at room temperature (~24°C) for 30 min before subjecting to HDX. For GDP AlF_4^- binding, dynamin was pre-incubated with NaF (10 mM) to which GDP (1 mM) and $AlCl_3$ (1 mM) were added and the reaction mix was incubated for 10 min at RT before HDX. For S619L HDX, 10 μM of $Dyn1^{WT}$ or $Dyn1^{S619L}$ was incubated at room temperature for 30 min and then subjected to HDX analysis comparing the two Apo proteins. To initiate deuterium exchange, the samples were diluted fivefold with D_2O-containing HDX buffer (20 mM HEPES 7.5, 150 mM KCl, 2 mM $MgCl_2$) and incubated at room temperature (~24°C) for 0 s, 60 s, or 900 s. Upon exchange, unwanted forward or back exchange was minimized and the protein was denatured by the addition of 25 μl of a quench solution (1% v/v TFA in 5 M urea and 50 mM TCEP, pH 2.5) and immediately flash-frozen. Post-quenching, the polypeptide was digested by passing through an immobilized pepsin column (prepared in house) and the resulting peptides were separated by HPLC and analyzed using a LTQ Orbitrap XL ETD mass spectrometer (Marciano *et al*, 2014). The percent deuterium exchange values for peptide isotopic envelopes at each time point were calculated and processed using the HDX Workbench Software, which measures *P*-values at individual time points to determine whether changes are statistically significant (Pascal *et al*, 2012).

HDX data are presented as an average of three independent triplicates. Deuterium uptake for each peptide in the perturbation heat map view is calculated as the average of % D_2O for the two time points (60 s and 900 s) and the difference in average % D_2O values between the *apo* and liganded states is presented as a heat map with a color code given at the bottom of each figure (warm colors for deprotection, cool colors for protection). Regions were colored only if they show a > 5% difference (less or more protection) between the two states and if at least one time point showed a statistically significant difference in a paired two-tailed Student's *t*-test ($P < 0.05$). Gray color represents no significant change (0–5%) between the two states. The exchange at the first two residues for any given peptide is rapid and is ignored in the calculations. Each peptide bar in the heat map view displays the average Δ %D_2O values with its associated standard deviation and the charge state shown in parentheses. To interpret the HDX data in cases of overlapping peptides with different color codes in the heat map, the conventional subtractive analysis approach of subtracting the difference of shorter peptides from longer peptides (Marciano *et al*, 2014) was used to narrow down the perturbation differences to specific regions of proteins (within a few amino acids).

Cell culture and dynamin reconstitution

Human H1299 non-small lung cancer cell lines (a gift from Dr. John Minna, UT Southwestern, Dallas, TX) were reconstituted with Dyn2-EGFP (WT or S619L) through retroviral infection using a pMIEG3 vector coding for Dyn2-EGFP designed to be resistant to siRNA by

© 2016 The Authors

introducing silent mutations at the target site. The cells were FACS-sorted for near endogenous expression. Cells were grown in RPMI media (Life Technologies) containing 5% FCS (HyClone). To suppress endogenous Dyn2, cells were transfected with siRNA specifically targeting endogenous Dyn2 (GACATGATCCTGCAGTT CATT) using Lipofectamine RNAiMAX (Life Technologies, Carlsbad, CA). Cells were harvested for imaging or uptake assay 90 h after siRNA treatment. Western blotting against Dyn2 (goat anti-Dyn2, Santa Cruz Biotech) confirmed the expression levels. ARPE19 cells were similarly infected with Dyn2 and Dyn2^{S619L} mutant encoding viruses and sorted for high expression levels. The mutant S619L was predominantly localized in large punctate vacuolar structures (see Fig EV5B) and hence was not used for further analysis.

Immunofluorescence and live cell imaging

H1299 (and ARPE19) cells were plated on gelatin-coated glass coverslips and allowed to adhere for 4 h. For immunofluorescence, cells were simultaneously fixed and permeabilized with 2% PFA and 0.5% Triton X-100 for 2 min followed by 30-min fixation with 4% PFA. Clathrin light chain (CLC) was labeled with mouse monoclonal antibody (sc-12735) or AP2 was labeled with AP6 mouse monoclonal antibody (Abcam) for co-localization studies with Dyn2-EGFP or Dyn2^{S619L}-EGFP. Fluorescence imaging was performed using a 100 × 1.49 NAA TIRF objective (Nikon) mounted on a Ti-Eclipse inverted microscope equipped with the Perfect Focus System (Nikon). For live cell imaging, H1299 cells were infected with CLC-Tdtomato adenovirus for 12 h for sufficient overexpression, prior to plating on gelatin-coated slides. Cells were plated on cover slides 2 h prior to imaging and were maintained in DMEM lacking phenol red and supplemented with 5% fetal calf serum. Sequential acquisition of time lapse images with 2-s intervals was performed with an exposure time of 100 ms using a CoolSNAP HQ2 mono-chrome CCD camera with 6.45 × 6.45 lm2pixels (Photometrics). Analysis of Dyn2-EGFP and CLC-Tdtomato-positive clathrin-coated pits and lifetimes of bona fide clathrin-coated pits were quantified using in-house software (Aguet *et al*, 2013).

Clathrin-mediated endocytosis and CCP dynamics

Transferrin receptor (TfnR) uptake, measured using accumulation of D65 antibody against TfnR, was performed using an in cell ELISA approach as previously described (Reis *et al*, 2015). TIRF-M-based assays and Master/Slave analyses were performed exactly as previously described (Aguet *et al*, 2013).

Expanded View for this article is available online.

Acknowledgements
We thank Marcel Mettlen and Juha-Pekka Mattila for helpful discussions. We also thank Oliver Daumke and Katja Faelber for communicating data on Dyn3 structure prior to publication. Wesley Burford and Aparna Mohanakrishnan provided technical assistance. This work was supported by National Institutes of Health Grant R01GM42455 and Welch Foundation Grant I-1823 to S.L.S.

Author contributions
SS, VD, PRG, and SLS designed experiments and analyzed data. SLS conceived and supervised the project. SS performed biochemical and cell-culture experiments. VD performed all deuterium exchange mass spectrometry experiments. DKR obtained electron micrographs of dynamin. SLS and SS wrote the manuscript with input from PRG and VD.

Conflict of interest
The authors declare that they have no conflict of interest.

Note added in proof
While this work was under production, another independent study reported a role for the $\alpha 2^S$ helix in transmitting PRD-SH3 mediated allosteric regulation of the G-domain (Krishnan S, Collett M, Robinson PJ (2015) SH3 domains differentially stimulate distinct dynamin I assembly modes and G domain activity. *PLoS One* 10: e0144609).

References

Aguet F, Antonescu CN, Mettlen M, Schmid SL, Danuser G (2013) Advances in analysis of low signal-to-noise images link dynamin and AP2 to the functions of an endocytic checkpoint. *Dev Cell* 26: 279 – 291

Bellacosa A, Chan TO, Ahmed NN, Datta K, Malstrom S, Stokoe D, McCormick F, Feng JN, Tsichlis P (1998) Akt activation by growth factors is a multiple-step process: the role of the PH domain. *Oncogene* 17: 313 – 325

Cao H, Garcia F, McNiven MA (1998) Differential distribution of dynamin isoforms in mammalian cells. *Mol Biol Cell* 9: 2595 – 2609

Carr JF, Hinshaw JE (1997) Dynamin assembles into spirals under physiological salt conditions upon the addition of GDP and gamma-phosphate analogues. *J Biol Chem* 272: 28030 – 28035

Chalmers MJ, Busby SA, Pascal BD, He YJ, Hendrickson CL, Marshall AG, Griffin PR (2006) Probing protein ligand interactions by automated hydrogen/deuterium exchange mass spectrometry. *Anal Chem* 78: 1005 – 1014

Chalmers MJ, Busby SA, Pascal BD, West GM, Griffin PR (2011) Differential hydrogen/deuterium exchange mass spectrometry analysis of protein-ligand interactions. *Exp Rev Proteomics* 8: 43 – 59

Chappie JS, Acharya S, Liu Y-W, Leonard M, Pucadyil TJ, Schmid SL (2009) An intramolecular signaling element that modulates dynamin function in vitro and in vivo. *Mol Biol Cell* 20: 3561 – 3571

Chappie JS, Acharya S, Leonard M, Schmid SL, Dyda F (2010) G domain dimerization controls dynamin's assembly-stimulated GTPase activity. *Nature* 465: 435 – 440

Chappie JS, Mears JA, Fang S, Leonard M, Schmid SL, Milligan RA, Hinshaw JE, Dyda F (2011) A pseudoatomic model of the dynamin polymer identifies a hydrolysis-dependent powerstroke. *Cell* 147: 209 – 222

Chappie JS, Dyda F (2013) Building a fission machine - structural insights into dynamin assembly and activation. *J Cell Sci* 126: 2773 – 2784

Chen YJ, Zhang P, Egelman EH, Hinshaw JE (2004) The stalk region of dynamin drives the constriction of dynamin tubes. *Nat Struct Mol Biol* 11: 574 – 575

Chernomordik LV, Kozlov MM (2003) Protein-lipid interplay in fusion and fission of biological membranes. *Ann Rev Bioch* 72: 175 – 207

Chin YH, Lee A, Kan HW, Laiman J, Chuang MC, Hsieh ST, Liu Y-W (2015) Dynamin-2 mutations associated with centronuclear myopathy are hypermorphic and lead to T-tubule fragmentation. *Hum Mol Genet* 24: 5542 – 5554

Cocucci E, Gaudin R, Kirchhausen T (2014) Dynamin recruitment and membrane scission at the neck of a clathrin-coated pit. *Mol Biol Cell* 25: 3595 – 3609

Durieux A-C, Prudhon B, Guicheney P, Bitoun M (2010) Dynamin 2 and human diseases. *J Mol Med* 88: 339 – 350

 © 2016 The Authors

Ehrlich M, Boll W, van Oijen A, Hariharan R, Chandran K, Nibert ML, Kirchhausen T (2004) Endocytosis by random initiation and stabilization of clathrin-coated pits. *Cell* 118: 591 – 605

Faelber K, Posor Y, Gao S, Held M, Roske Y, Schulze D, Haucke V, Noe F, Daumke O (2011) Crystal structure of nucleotide-free dynamin. *Nature* 477: 556 – 560

Ferguson SM, De Camilli P (2012) Dynamin, a membrane-remodelling GTPase. *Nat Rev Mol Cell Biol* 13: 75 – 88

Ford MG, Jenni S, Nunnari J (2011) The crystal structure of dynamin. *Nature* 477: 561 – 566

Horn JR, Kraybill B, Petro EJ, Coales SJ, Morrow JA, Hamuro Y, Kossiakoff AA (2006) The role of protein dynamics in increasing binding affinity for an engineered protein-protein interaction established by H/D exchange mass spectrometry. *Biochemistry* 45: 8488 – 8498

Jeganathan S, von Bergen M, Brutlach H, Steinhoff HJ, Mandelkow E (2006) Global hairpin folding of tau in solution. *Biochemistry* 45: 2283 – 2293

Kenniston JA, Lemmon MA (2010) Dynamin GTPase regulation is altered by PH domain mutations found in centronuclear myopathy patients. *EMBO J* 29: 3054 – 3067

Lemmon MA (2007) Pleckstrin homology (PH) domains and phosphoinositides. *Cell Biol Inositol Lipids Phosphates* 74: 81 – 93

Leonard M, Song BD, Ramachandran R, Schmid SL (2005) Robust colorimetric assays for dynamin's basal and stimulated GTPase activities. *Methods Enzymol* 404: 490 – 503

Liu Y-W, Neumann S, Ramachandran R, Ferguson SM, Pucadyil TJ, Schmid SL (2011) Differential curvature sensing and generating activities of dynamin isoforms provide opportunities for tissue-specific regulation. *Proc Natl Acad Sci USA* 108: E234 – E242

Marciano DP, Dharmarajan V, Griffin PR (2014) HDX-MS guided drug discovery: small molecules and biopharmaceuticals. *Curr Opin Struct Biol* 28: 105 – 111

Mattila JP, Shnyrova AV, Sundborger AC, Hortelano ER, Fuhrmans M, Neumann S, Muller M, Hinshaw JE, Schmid SL, Frolov VA (2015) A hemi-fission intermediate links two mechanistically distinct stages of membrane fission. *Nature* 524: 109 – 113

Mears JA, Ray P, Hinshaw JE (2007) A corkscrew model for dynamin constriction. *Structure* 15: 1190 – 1202

Mehrotra N, Nichols J, Ramachandran R (2014) Alternate pleckstrin homology domain orientations regulate dynamin-catalyzed membrane fission. *Mol Biol Cell* 25: 879 – 890

Morlot S, Roux A (2013) Mechanics of dynamin-mediated membrane fission. *Ann Rev Biophys* 42: 629 – 649

Neumann S, Pucadyil TJ, Schmid SL (2013) Analyzing membrane remodeling and fission using supported bilayers with excess membrane reservoir. *Nat Protoc* 8: 213 – 222

Pascal BD, Willis S, Lauer JL, Landgraf RR, West GM, Marciano D, Novick S, Goswami D, Chalmers MJ, Griffin PR (2012) HDX workbench: software for the analysis of H/D exchange MS data. *J Am Soc Mass Spectrom* 23: 1512 – 1521

Praefcke GJK, McMahon HT (2004) The dynamin superfamily: universal membrane tubulation and fission molecules? *Nat Rev Mol Cell Biol* 5: 133 – 147

Ramachandran R, Surka M, Chappie JS, Fowler DM, Foss TR, Song BD, Schmid SL (2007) The dynamin middle domain is critical for tetramerization and higher-order self-assembly. *EMBO J* 26: 559 – 566

Ramachandran R, Schmid SL (2008) Real-time detection reveals that effectors couple dynamin's GTP-dependent conformational changes to the membrane. *EMBO J* 27: 27 – 37

Ramachandran R, Pucadyil TJ, Liu Y-W, Acharya S, Leonard M, Lukiyanchuk V, Schmid S (2009) Membrane insertion of the pleckstrin homology domain variable loop 1 is critical for dynamin-catalyzed vesicle scission. *Mol Biol Cell* 20: 4630 – 4639

Reis CR, Chen PH, Srinivasan S, Aguet F, Mettlen M, Schmid SL (2015) Crosstalk between Akt/GSK3beta signaling and dynamin-1 regulates clathrin-mediated endocytosis. *EMBO J* 34: 2132 – 2146

Reubold TF, Faelber K, Plattner N, Posor Y, Ketel K, Curth U, Schlegel J, Anand R, Manstein DJ, Noe F, Haucke V, Daumke O, Eschenburg S (2015) Crystal structure of the dynamin tetramer. *Nature* 525: 404 – 408

Scheffzek K, Welti S (2012) Pleckstrin homology (PH) like domains - versatile modules in protein-protein interaction platforms. *FEBS Lett* 586: 2662 – 2673

Schmid SL, Frolov VA (2011) Dynamin: functional design of a membrane fission catalyst. *Ann Rev Cell Dev Biol* 27: 79 – 105.

Shnyrova AV, Bashkirov PV, Akimov SA, Pucadyil TJ, Zimmerberg J, Schmid SL, Frolov VA (2013) Geometric catalysis of membrane fission driven by flexible dynamin rings. *Science* 339: 1433 – 1436

Solomaha E, Palfrey HC (2005) Conformational changes in dynamin on GTP binding and oligomerization reported by intrinsic and extrinsic fluorescence. *Biochem J* 391: 601 – 611

Srinivasan S, Mattila J-P, Schmid SL (2014) Intrapolypeptide interactions between the GTPase effector domain (GED) and the GTPase domain form the bundle signaling element in dynamin dimers. *Biochemistry* 53: 5724 – 5726

Sundborger AC, Fang S, Heymann JA, Ray P, Chappie JS, Hinshaw JE (2014) A Dynamin Mutant Defines a Superconstricted Prefission State. *Cell Rep* 8: 734 – 742

Taylor MJ, Lampe M, Merrifield CJ (2012) A feedback loop between dynamin and actin recruitment during clathrin-mediated endocytosis. *PLoS Biol* 10: e1001302

© 2016 The Authors